Title
The offshore boundary condition in surf zone modeling

Journal
Coastal Engineering, 143

ISSN
03783839

Authors
Fiedler, Julia W
Smit, Pieter B
Brodie, Katherine L
et al.

Publication Date
2019

DOI
10.1016/j.coastaleng.2018.10.014

Data Availability
The data associated with this publication are available upon request.

Peer reviewed

The offshore boundary condition in surf zone modeling

Julia W. Fiedler[a,*], Pieter B. Smit[b], Katherine L. Brodie[c], Jesse McNinch[c], R. T. Guza[a]

[a]*Scripps Institution of Oceanography, La Jolla, California*
[b]*Spoondrift*
[c]*Coastal & Hydraulics Laboratory, U.S. Army Engineer Research and Development Center, Duck, NC*

Abstract

Numerical models predicting surfzone waves and shoreline runup in field situations are often initialized with shoreward propagating (sea-swell, and infragravity) waves at an offshore boundary in 10-30 m water depth. We develop an offshore boundary condition, based on Fourier analysis of observations with co-located current and pressure sensors, that accounts for reflection and includes nonlinear phase-coupling. The performance of additional boundary conditions derived with limited or no infragravity observations are explored with the wave resolving, nonlinear model SWASH 1D. In some cases errors in the reduced boundary conditions (applied in 11m depth) propagate shoreward, whereas in other cases errors are localized near the offshore boundary. Boundary conditions that can be implemented without infragravity observations (e.g. bound waves) do not accurately simulate infragravity waves across the surfzone, and could corrupt predictions of morphologic change. However, the bulk properties of infragravity waves in the inner surfzone and runup are predicted to be largely independent of ig offshore boundary conditions, and dominated by ig generation and dissipation.

Keywords: boundary conditions, bispectral analysis, numerical modeling, infragravity waves

---

*Corresponding author
Email address: `jfiedler@ucsd.edu` (Julia W. Fiedler)

1. Introduction

Infragravity (ig) waves, with frequencies nominally between 0.004-0.04Hz on Pacific ocean coasts, can significantly influence surfzone morphology (e.g. de Bakker et al., 2016, and references therein) and shoreline runup and inundation (e.g. Stockdon et al., 2006; Ruggiero et al., 2004). Using nonlinear perturbation analysis, Longuet-Higgins and Stewart (1962) and Hasselmann (1962) showed the theoretical existence of ig equilibrium bound waves, locally forced by quadratic interactions of two sea-swell (ss) frequency waves. With equilibrium bound waves, sea-swell wave groups and ig waves are 180° out of phase, and sea-swell and infragravity wave energies and biphases are unchanging in constant depth.

In laboratory flumes with unidirectional waves (e.g. 1D), the bound wave solution is often imposed using wavemaker motion corrections that suppress generation of free shoreward propagating ig waves (Kostense, 1985), and absorb seaward propagating ig waves. Numerical modeling of laboratory studies often include bound ig waves at the offshore boundary by default (e.g. Rijnsdorp et al., 2014; de Bakker et al., 2015). In highly controlled laboratory flumes, carefully implemented numerical models agree well with observations, and the models provide insight into the complex physics of ig waves in the surfzone and runup (Torres-Freyermuth et al., 2010; de Bakker et al., 2014, 2015; Ruju et al., 2014).

Higuera et al. (2013a,b, 2015) considered unidirectional and directional laboratory wave generation in careful detail, including absorbing side walls and second order corrections. However, the cases considered were either transient groups, or unidirectional, monochromatic waves on a beach with a channel. Orszaghova et al. (2014) showed significant differences in runup resulted when an isolated incident wave group included, and did not include, 2nd order nonlinear effects at the offshore wavemaker. Offshore boundary conditions for the case of frequency and direction spread (2D) incident waves breaking on a sloping, potentially reflective beach were not considered. This geometry supports topographic edge waves – resonances that further complicate 2D boundary conditions.

Runup on ocean beaches is more complicated than in a wave flume (1D) or wave basin (2D) for several reasons. Bound wave solutions lose validity with increasing nonlinearity, and shoreward propagating, directionally spread free ig waves, not phase coupled to ss waves, often dominate the observed infragravity energy in 10-30 m depth where models are initialized. Shoreward propagating free ig waves can arrive at these depths from distant sources (Bromirski et al., 2010; Ardhuin et al., 2014), topographic trapping of ig waves that have reflected off local beaches (Herbers et al., 1995; Smit et al., 2018), or shoaling short wave groups. Furthermore, the full frequency-directional spectrum of ss and ig waves required to initialize 2D models are rarely known. In region-wide predictions of shoreline runup, the sea-swell frequency directional spectra at the offshore boundary are obtained from wind wave generation and propagation models (e.g. SWAN) that do not include relevant nonlinear ig wave dynamics. Compounding the lack of boundary information, models may be initialized with data from offshore wave buoys, which lack the low frequency dynamic response needed to measure ig waves (Mccall et al., 2014; Gomes et al., 2016; Nicolae Lerma et al., 2017). Lacking alternatives, boundary conditions for shoreward propagating ig waves have included equilibrium (1D and 2D) solutions (e.g. Van Dongeren et al., 2012; Mccall et al., 2014) or assumed zero ig energy at the boundary (van Rooijen et al., 2016). More often, model predictions of runup do not explicitly describe the ig boundary condition (e.g. Guimarães et al., 2015; Gomes et al., 2016; Gallien, 2016; Nicolae Lerma et al., 2017).

Here, the effect of different offshore boundary conditions for ss and ig waves are explored with the phase-resolving numerical model SWASH (v 4.01), a multilayer non-hydrostatic model that supports a range of offshore boundary conditions, including bound waves (Zijlema et al., 2011). Linear and nonlinear implementations of pressure data only, and of co-located pressure-current data, are compared at the offshore boundary. A bound infragravity wave assumption, which can be implemented without infragravity observations at the boundary, is also discussed. The field site and test cases are described in Section 2. Analysis methods are discussed in Section 3. Six offshore boundary conditions (Section 4) are examined both at the offshore boundary (Section 5) and further shoreward (Section 6). Conclusions are in Section 7.

2. Observations, quality control and test cases

Wave evolution was observed at the gently sloped (between 1/50 and 1/70) Agate Beach, Oregon for two months during Fall 2013 (Fiedler et al., 2015). Significant wave heights ranged from 0.5 m to 7.5 m at NDBC buoy 46050, located 37 km offshore in 128 m water depth. The tide range was $\sim$ 2 m. Co-located pressure and current meters (PUVs) were deployed on a cross-shore transect spanning roughly 1.2 km (Figure 1). Wave runup, co-incident with the instrumented transect, was measured with a cliff-mounted, scanning lidar. Bathymetry was measured on cross-shore transects from the back beach to the offshore sensor using a GPS-equipped all-terrain vehicle, hand-pushed dolly, and a sonar-mounted jet-ski.

PUV data were quality-controlled for shore-normality, biofouling or other distortions from the expected linearity, and the presence of eddy motions. In retained observations, the ratio of variance of wave-induced pressure to horizontal velocity differed from the linear value by less than 30% (Herbers et al., 1999). Shore-normal propagation was enforced with a restricted ratio of significant alongshore to cross-shore high ig frequency band (0.025-0.04 Hz) squared velocities (V_{ig}^2/U_{ig}^2); ratios exceeding 0.55 with along- or cross-shore velocities greater than 1 cm/s were rejected. Lastly, to exclude eddy motions not associated with sea surface fluctuations, records were rejected if the ratio of excess kinetic energy to potential energy at ig frequencies (Lippmann et al., 1999) exceeded 0.25. While all the data at the deepest (11m) gauge PUV8 passed quality control, shoreward sensors sometimes failed. For instance, during the highest-wave test case below, three inner-surf zone sensors were non-operational or failed quality control tests. Each quality control test was failed at least once. Runup observations with excessive noise from long-range (400 m) sampling, wind, rain and fog, were rejected (Fiedler et al., 2015).

In the 19 one-hour-long test cases, wave height at the deepest (11 m depth) pressure sensor PUV8 ranged 1.2–4.7 m, peak frequency 0.06–0.1 Hz, and tide level 1.1–2.4 m NAVD88. Infragravity energy at PUV8 was not tidally modulated, in contrast to observations at other beaches. With the most energetic ss waves, PUV8 was within the surfzone. The bulk nonlinearity, characterized by the Ursell number (Ursell, 1952)

$$\mathrm{Ur} = \frac{a/h}{(kh)^2} \tag{1}$$

varied between 0.05-0.4, where a is wave amplitude $H_{\mathrm{sig}}/2$, h is water depth, and k a mean wavenumber, derived with the linear dispersion relationship.

Infragravity (0.004–0.04 Hz) and sea-swell (0.04–0.25 Hz) band-integrated contributions (second order moments) are used to estimate band reflections R_{ig}^2 and R_{ss}^2 at PUV8, where

$$R_{\mathrm{ig}}^2 = F_{\mathrm{ig}}^{+}/F_{\mathrm{ig}}^{-}, \tag{2}$$

with $F^{\pm}$ as energy flux. $F^{\pm}$ is estimated with pressure and cross-shore velocity measurements at the boundary (Sheremet et al., 2005),

$$F_{\mathrm{ig}}^{\pm} = E_{\mathrm{ig}}^{\pm}|C_{\mathrm{x}}|, \tag{3}$$

where $|C_x|$ is the cross-shore group speed (linear theory) and

$$E^{\pm}(f,x) = \frac{1}{4}\left(S_{\mathrm{PP}}(f,x) + \frac{h^2}{C_{\mathrm{x}}^2}S_{\mathrm{UU}}(f,x) \pm 2\frac{h}{|C_{\mathrm{x}}|}\Re\{S_{\mathrm{PU}}(f,x)\}\right), \tag{4}$$

where S_{PP} and S_{UU} are autospectra of ig-frequency pressure and velocity, and $\Re\{S_{\mathrm{PU}}\}$ is the real part of the pressure-velocity cross spectrum.

Agate is low sloped, and $R_{\mathrm{ss}}^2 < 0.01$ at PUV8 for all cases (not shown). R_{ig}^2 ranged from 0.1-1.0 (Figure 2a). With energetic ss waves, ig waves primarily propagate onshore (e.g. when $H = 4.5$ m, Ur~ 0.4, $R_{\mathrm{ig}}^2 \sim 0.1$). In contrast, with lower ss energy ($H = 1.2$ m, Ur~ 0.05), shoreward and seaward fluxes are approximately equal ($R_{\mathrm{ig}}^2 \sim 1$).

3. Third order statistics

Spectral and bispectral analysis are commonly used to describe second and third order moments, by analyzing the statistics of a wave field in the frequency domain (Hasselmann, 1962; Kim and Powers, 1979; Elgar and Guza, 1985a,b; Herbers and Burton, 1997; Thomson et al., 2006; Guedes et al., 2013; Pequignet et al., 2014; de Bakker et al., 2015, and many others). Specifically, bulk variance, skewness and asymmetry are obtained from appropriate integration over the spectrum and/or bispectrum. Extracting particular correlations between the ig and ss band requires diligent definition of integration domain of the bispectrum (e.g. de Bakker et al., 2015). Alternatively, third order statistics may be computed in the time domain. Decomposing the demeaned sea surface η into infragravity ig (0.004-0.04 Hz) and sea-swell ss (0.04-0.25 Hz) components $\eta = \eta_{\mathrm{ig}} + \eta_{\mathrm{ss}}$ yields

$$\langle \eta^2 \rangle = \langle \eta_{\mathrm{ig}}^2 \rangle + \langle \eta_{\mathrm{ss}}^2 \rangle \tag{5}$$

where $\langle \ldots \rangle$ is the time average. The variance is simply the sum of ig and ss components (5), whereas the skewness also contains interaction terms

$$\mathrm{Sk} \equiv \langle \eta^3 \rangle = \langle \eta_{\mathrm{ss}}^3 \rangle + 3\langle \eta_{\mathrm{ig}} \eta_{\mathrm{ss}}^2 \rangle + 3\langle \eta_{\mathrm{ss}} \eta_{\mathrm{ig}}^2 \rangle + \langle \eta_{\mathrm{ig}}^3 \rangle. \tag{6}$$

Here $\mathrm{Sk}_{\mathrm{ss,ss,ss}} = \langle \eta_{\mathrm{ss}}^3 \rangle$ and $\mathrm{Sk}_{\mathrm{ig,ig,ig}} = \langle \eta_{\mathrm{ig}}^3 \rangle$ are skewness values associated with the individual bands. Further, $\mathrm{Sk}_{\mathrm{ig,ss,ss}} = 3\langle \eta_{\mathrm{ig}} \eta_{\mathrm{ss}}^2 \rangle$ essentially describes correlation between ss wave amplitude modulation and waves in the ig-band, and is of prime interest here. The second interaction term $\mathrm{Sk}_{\mathrm{ig,ig,ss}} = 3\langle \eta_{\mathrm{ig}}^2 \eta_{\mathrm{ss}} \rangle$ describes sum correlation of ig waves and a (nonlinearly forced) harmonic in the ss-band. These correlations are only significant in the surf-zone (where ig-waves become nonlinear, e.g. prior to breaking) and are not further considered here. Similarly, defining asymmetry as $\mathrm{As} = \langle \mathcal{H}\{\eta\}^3 \rangle$, where $\mathcal{H}\{n\}$ is the Hilbert transform of η,

$$\mathrm{As} = \mathrm{As}_{\mathrm{ss,ss,ss}} + \mathrm{As}_{\mathrm{ig,ss,ss}} + \mathrm{As}_{\mathrm{ig,ig,ss}} + \mathrm{As}_{\mathrm{ig,ig,ig}}. \tag{7}$$

Apart from practical differences introduced due to statistical chatter and spectral analysis, integrated parameters obtained from decompositions calculated in the time-domain are equivalent to those obtained from bispectral analysis, but typically more convenient to calculate. Further, by representing the demeaned sea surface as the complex analytic signal

$$\zeta = \eta + i\mathcal{H}\{n\},$$

and introducing a decomposition into ig and ss bands as before ($\zeta = \zeta_{\mathrm{ig}} + \zeta_{\mathrm{ss}}$), skewness and asymmetry can be succinctly described by complex third order moments of ζ. In particular, we find

$$\begin{aligned}
\mathrm{Sk}_{\mathrm{ss,ss,ss}} + i\mathrm{As}_{\mathrm{ss,ss,ss}} &= \frac{3}{4}\langle \zeta_{\mathrm{ss}}\zeta_{\mathrm{ss}}\zeta_{\mathrm{ss}}^{*}\rangle,\\
\mathrm{Sk}_{\mathrm{ig,ss,ss}} + i\mathrm{As}_{\mathrm{ig,ss,ss}} &= \frac{3}{2}\langle \zeta_{\mathrm{ig}}\zeta_{\mathrm{ss}}\zeta_{\mathrm{ss}}^{*}\rangle,\\
\mathrm{Sk}_{\mathrm{ig,ig,ig}} + i\mathrm{As}_{\mathrm{ig,ig,ig}} &= \frac{3}{4}\langle \zeta_{\mathrm{ig}}\zeta_{\mathrm{ig}}\zeta_{\mathrm{ig}}^{*}\rangle,
\end{aligned}$$

where skewness and asymmetry are associated with real or imaginary parts of the complex third order moments. Further, analogous to the definition of the biphase as the argument of the bispectrum, the biphase associated with the correlation between wave groups and ig-waves can be defined as

$$\phi_{\mathrm{ig,ss,ss}} = \tan^{-1}\frac{\mathrm{As}_{\mathrm{ig,ss,ss}}}{\mathrm{Sk}_{\mathrm{ig,ss,ss}}}. \tag{8}$$

Similarly, $\phi_{\mathrm{ss,ss,ss}}$ is the biphase of η_{ss}^3. The shape of individual short and long waves are described by $\phi_{\mathrm{ss,ss,ss}}$ and $\phi_{\mathrm{ig,ig,ig}}$. Peaky and pitched-forward waves have biphases of 0° and 90°, respectively (Masuda and Kuo, 1981).

When the highest waves in an ss group coincide with the crest of an ig wave, the constructively superposed crests create $\mathrm{Sk}_{\mathrm{ig,ss,ss}} > 0$. With an equilibrium bound wave, the largest short waves are in a long wave trough, and constructively superposed troughs yield $\mathrm{Sk}_{\mathrm{ig,ss,ss}} < 0$ (Figure 3a). At PUV8, $\mathrm{Sk}_{\mathrm{ig,ss,ss}}$ is increasingly negative with increasing Ur (Figure 2b). Of several plausible options, we use a $\mathrm{Sk}_{\mathrm{ig,ss,ss}}$ normalization that, similar to bicoherence, is constrained between -1 and 1 (equation A.5, see Appendix A for details).

4. Model boundary conditions

Deterministic nearshore wave models require a phase-resolved description of the incident wave field along the entire forcing boundary with velocities and surface elevation. However, typically only estimates of the directional sea/swell spectrum E_{ss} are available, and the ss signal is constructed by assigning uniformly random phases and formally Rayleigh distributed amplitudes to binned intervals of the spectrum, whereas free contributions to η_{ig} are neglected by necessity (E_{ig} is unknown). If the waves are moderately steep and in intermediate to deep water, weak nonlinearity (bound response) may be included by use of equilibrium theory. However, due to computational and logistical constraints, surfzone and runup models are typically initialized at moderate depths (10–30 m) where free ig-waves can contribute significantly and equilibrium theory can break down with high Ursell number (e.g. resonance or near-resonance). Infragravity boundary conditions based on E_{ss} alone are problematic. It is unclear whether it is worse to neglect shoreward propagating ig waves at the offshore boundary ($E_{\mathrm{ig}} = 0$), or to include potentially erroneous bound wave estimates.

PUV observations of near-bottom pressure and wave velocities potentially give increased information on non-linearity and ig-characteristics although only limited directional information can be inferred. The assumption of 1D cross-shore dynamics is reasonable for ss-band waves if observations are in close proximity to shore. Although ig-waves observed on the inner shelf are often closer to omni- than uni-directional (e.g. Herbers et al., 1995), in lieu of better alternatives we use 1D ig-dynamics. Frequency spectra E_{ss} and E_{ig} derived from the pressure signal P provides non-directional estimates. Including cross-shore current (U) measurements allow separation of incident and reflected waves, sometimes significant in the ig-band (ss-band reflection is usually negligible on low slope beaches). Consequently, with local pressure and velocity observations we can compare estimates based on E_{ss} alone (using equilibrium theory, or $E_{\mathrm{ig}} = 0$), to a linear estimate of η_{ig} derived from P assuming free wave ig-dynamics where we optionally remove reflected waves from the signal in the ig-band. We refer to these various options as Boundwave, $E_{\mathrm{ig}} = 0$, Free P, and Free PU boundaries, respectively, wherein sea-swell phases are randomized to simulate a spectral input to the boundary (Table 1).

Table 1: Tested boundary conditions

	BC	IG (0.004-0.04 Hz)	SS (0.04-0.25 Hz)	Reflection[a]	Nonlinearity[b]		
					SS	IG	SS-IG
(1)	Boundwave	2nd order equilibrium bound solution	P, random phases	no	no	no	yes
(2)	$E_{\mathrm{ig}} = 0$	zero IG energy	P, random phases	no	no	no	no
(3)	Free P	P, random phases	P, random phases	no	no	no	no
(4)	Fourier P	P, observed phases	P, observed phases	no	yes	yes	yes
(5)	Free PU	PU, random phases	P, random phases	yes	no	no	no
(6)	Fourier PU	PU, observed phases	P, observed phases	yes	yes	yes	yes

[a] Combined P and U allow for removal of reflected waves.

[b] Nonlinearity is divided into three nonlinear phase-coupling groups; sea-swell only (SS), infragravity only (IG), and interaction nonlinearity between the two frequency bands (SS-IG).

As shown below, boundary conditions assuming random phases are problematic when phases are nonlinearly coupled. For example, the peaky and pitched forward (skewed and asymmetric) shapes of shoaled waves are not reproduced with random ss phases. Although the Boundwave BC (Model 1 in Table 1) includes interaction nonlinearity between ig and ss, the assumption of a passive bound response of ig waves to incident wave groups is usually violated. Only Fourier methods (Models 4,6 in Table 1) include phase coupling in all frequency bands; the model can be directly driven with phases derived from a Fourier series representation of the observations. In shallow water a linear reconstruction of surface amplitudes from pressure is sufficient to obtain second order accuracy in non-linearity, although reconstruction of normal velocities does require higher order corrections. Further, if the reflected signal is assumed small, P and

U observations can be used to remove reflected contributions from the signal (referred to as Fourier PU boundary; see Table 1). The Fourier PU boundary condition preserves nonlinear coupling present in the observed shoreward propagating components of the observations.

To evaluate the performance of different boundary conditions, the model domain extends from the most offshore sensor PUV8 to the landward edge of the swash zone, with variable cross-shore grid spacing decreasing from $dx = 3\,\mathrm{m}$ offshore to $dx = 1\,\mathrm{m}$ in the swash zone (see Fiedler et al. (2018) for details). Two layers, default numerics, and default breaking and friction coefficients, are used. These suffice to evaluate different boundary conditions, as well as error propagation away from the boundary. To match the one-hour-long test cases, model data were collected for 1 hour after 10 minutes of spin up. Each simulation took approximately 30 minutes to run on a laptop computer.

5. Results at the offshore boundary

Pressure-derived BCs (Free P, Fourier P) neglect reflection and overestimate the incoming energy flux by roughly R^2_{ig} (Figure 4), about a factor of 2 for the largest $R^2_{\mathrm{ig}} \sim 1$. Boundary conditions that include velocity (Free PU, Fourier PU) include reflection, but overestimate the observed shoreward flux slightly ($\sim 13\%$ average), due to neglected wave directionality. With the highest incident energy (strongest nonlinearity, $\mathrm{Ur} \sim 0.4$), the 1D bound wave BC overestimates the observed shoreward energy flux by ~ 9 (not shown). Bound wave (including 2D, not shown) errors are sometimes large owing to the presence of free ig waves and/or violation of the equilibrium bound wave assumptions $\mathrm{Ur} \ll 1$.

The largest skewness terms at the boundary, $\mathrm{Sk}_{\mathrm{ss,ss,ss}} = \langle \eta^3_{\mathrm{ss}} \rangle$ and the ig-ss-ss interaction term $\mathrm{Sk}_{\mathrm{ig,ss,ss}} = 3\langle \eta_{\mathrm{ig}} \eta^2_{\mathrm{ss}} \rangle$ are well reproduced by BCs retaining the measured phase relationships (Fourier P and Fourier PU, Figure 5a,c). Free wave BC, assume $\mathrm{Sk}_{\mathrm{ss,ss,ss}} = \mathrm{Sk}_{\mathrm{ig,ss,ss}} = 0$. The $E_{\mathrm{ig}} = 0$ BC also assumes $\mathrm{Sk}_{\mathrm{ss,ss,ss}} = 0$, but is undefined for $\mathrm{Sk}_{\mathrm{ig,ss,ss}}$. Fourier PU is overall the best of these boundary conditions. With the largest waves, $R^2_{\mathrm{ig}} \ll 1$ and Fourier P performs about as well as Fourier PU for skewness but still slightly overestimates the ig energy flux at the boundary (Figure 4 and 5a,c).

6. Boundary error propagation

The influence of different boundary-forcing is examined for 19 cases at PUV5 in 5 m depth, midway between PUV8 and the shoreline (Figure 5) and for two cases of contrasting high and moderate energy (Figure 6; Case 12; $H = 1.52$ m, Ur= 0.05, $R^2_{\mathrm{ig}} \sim 1$, and Case 1; $H = 4.2$ m, Ur= 0.4, and $R^2_{\mathrm{ig}} \sim 0.1$). In Case 12, the ss surfzone begins in 3 m water depth near $x = -600$ m, while in Case 1 waves are breaking at PUV8, in roughly 11 m depth (vertical gray line, Figure 6a,b).

Two BC (1, Bound and 2, $\mathrm{E}_{\mathrm{ig}} = 0$) can be applied without ig observations at the boundary. Bound waves can overestimate shoreward propagating ig energy with large Ur, and this overestimation persists to the inner surfzone (blue line, Figure 6d), although $\mathrm{Sk}_{\mathrm{ig,ss,ss}}$ for Case 1 is well-represented starting approximately 100 m into the domain (blue line, Figure 6k). More generally, the bound wave BC performs moderately well for bulk wave heights (e.g. blue line, Figure 6c) but overestimates the skewness through the mid-surfzone (Figure 5b). For Case 12, the misfit persists until roughly $x = -500$ m, or about 2 m water depth.

The underestimation of H_{ig} with the BC $E_{\mathrm{ig}} = 0$ is corrected within 400 m (red line, Figure 6c,d). Immediately onshore of the boundary, $\phi_{\mathrm{ig,ss,ss}}$ is slightly greater than $\pi/2$, in contrast to the observed $\phi_{\mathrm{ig,ss,ss}}$ of slightly less than π (red line, Figure 6g,m). This biphase difference is consistent with continued energy transfer from the sea-swell waves to the infragravity band by triad interactions (Herbers and Burton, 1997; de Bakker et al., 2015). The rapid over-adjustment and subsequent under-prediction of the biphase does not correct itself until much shallower water.

Fiedler et al. (2018) suggest that the 1D Bound BC can be used for bulk runup estimates, lacking ig boundary observations. The present results also suggest convergence of $E_{\mathrm{ig}} = 0$ toward a common solution in the inner surf zone.

As discussed in section 6.3, similar bulk runup statistics are predicted using all offshore BC (1-6 in Table 1), with differences between BC comparable to differences in a single BC with varying friction coefficient. Although 1D Bound and $E_{\mathrm{ig}} = 0$ can yield useful runup predictions, these BC do not accurately simulate infragravity waves across the entire surfzone, potentially corrupting predictions of morphologic change.

Infragravity observations are required for the remaining BCs (3-6). Nonzero $\mathrm{Sk}_{\mathrm{ig,ss,ss}}$ are predicted to evolve from the initially Gaussian distributions of the free wave BCs. After reaching 5 m water depth, skewness values are closer to observations than initially, but still differ significantly (Figure 5b). Recovery from boundary condition errors for the relatively long wavelength ig waves is incomplete, and slower than for the shorter ss waves (compare Figure 5b with 5d).

Sediment transport is often assumed directly proportional or related to the wave skewness or asymmetry (Bailard and Inman, 1981; Hoefel and Elgar, 2003, and many others). At the offshore boundary, $E_{\mathrm{ss}} >> E_{\mathrm{ig}}$ and unnormalized $\mathrm{Sk}_{\mathrm{ig,ss,ss}}$ is always less than unnormalized $\mathrm{Sk}_{\mathrm{ss,ss,ss}}$ (normalized moments are shown in Figure 6). For both the moderate and energetic wave cases, at the offshore boundary the ratio of unnormalized ($\mathrm{Sk}_{\mathrm{ig,ss,ss}}/\mathrm{Sk}_{\mathrm{ss,ss,ss}}$) is about -0.25. Near the shoreline, ig waves are relatively more important than offshore, and $\mathrm{Sk}_{\mathrm{ig,ss,ss}}/\mathrm{Sk}_{\mathrm{ss,ss,ss}}$ is 0.5 and 5.5 for the moderate and energetic cases, respectively. With energetic incident waves, $\mathrm{Sk}_{\mathrm{ig,ss,ss}} \gg \mathrm{Sk}_{\mathrm{ss,ss,ss}}$ and the ig-ss-ss interaction is crucial to accurate modeling of sediment transport.

Closer to the shoreline, local nonlinear processes largely collapse all BC solutions to the observations. With both high and low ss waves, and with all BC, the interaction biphase $\phi_{\mathrm{ig,ss,ss}}$ evolves rapidly near the shoreline, where it crosses 0 (short wave group crests occur at long wave crests) in shallow waters and hovers between 0 and $\pi/2$. The consequences of this biphase evolution to runup requires further exploration. As shown in section 6.3, similar bulk runup statistics are predicted by all offshore BC.

6.1. Infragravity-band adjustment lengths

Previous results show that methods retaining phase information (Fourier P, Fourier PU) are preferable if observations are available. In practice phase-resolved observations are often unavailable, and consequently insight into adjustment length-scales is desirable. Here we will define the adjustment length scale as the distance from the boundary where ig-energy levels, set by $E_{\mathrm{ig}} = 0$, recovered to within 5% of the values obtained with the Fourier PU BC. With the exception of one test case that did not recover from the original E_{ig} deficit until very shallow water and which is hereafter excluded, the observed ig equalization distances vary within 150-650 m of the boundary (e.g. Figure 6c,d). Note that because ig dynamics are nonlinear, $E_{\mathrm{ig}} = 0$ at the boundary does not necessarily produce the lowest E_{ig} at onshore locations. In some individual cases H_{ig} with different offshore BC first converge, and then diverge near the shoreline (Figure 6c). Runup, considered for all cases, is not sensitive to the BC (Figure 7) .

Inserting infragravity energy fluxes into a nonlinear energy balance (as in Henderson et al., 2006; Fiedler et al., 2015) confirms that energy growth in the ig band is due to triad interactions. Hence, apparent recovery is principally driven by nonlinear interactions. Even so, the cases considered display no systematic dependence of the adjustment length on the Ursell number (not shown). The recovery distance is inversely dependent on peak frequency (r^2=0.35) and spectral narrowness Q_B (r^2=0.42), where $Q_B = (T_{m,0,2}/T_{m,-1,0})^2$ (Rogers and Van Vledder, 2013). These parameters are mutually correlated, however, and the limited simulations presented here do not allow us to extend these results to general conclusions.

6.2. Sea-swell band

Though focus has been on ig-band dynamics, errors in the the ss-band skewness near the boundary can be large for boundaries that do not include observed phase-information. However, for the ss-band, the wave field rapidly relaxes to a more natural state, and observable differences are localized within a few 100 m of the offshore boundary - even for large Ur and breaking ss waves at the offshore boundary (blue and red lines, Figure 6n). In general, the ss biphase $\phi_{\mathrm{ss,ss,ss}}$ is near 0 (peaky) offshore of $x \sim -800\,\mathrm{m}$, and then drifts toward $-\pi/2$ (pitched forward) (Figure 6j,p). Sea-swell wave evolution approaching a pitched forward shape, independent of initial phases, has been previously noted in similar depths and wave conditions (e.g. Elgar and Guza, 1985a,b). Sea-swell waves are always weakly reflected at Agate, so P and PU methods yield similar results.

At the offshore boundary, SWASH bound-wave forcing at present excludes bound sum interactions, explaining the Gaussian sea-swell statistics ($\mathrm{Sk}_{\mathrm{ss,ss,ss}} = 0$, in blue, Figure 5c, Figure 6h,n). Sea-swell skewness values estimated from 2nd order equilibrium (e.g. Stokes) theory using observed spectra agree well with observed values (not shown). Inclusion in a future SWASH revision would correct these boundary discrepancies, but is unlikely to significantly affect results otherwise. Nonlinear sum interactions quickly relax the ss-band third-order statistics toward the natural state, and memory of erroneous boundary conditions is short for ss waves. Given otherwise indistinguishable short wave evolution (6a,b), enforcing a Gaussian state at the boundary does not significantly influence the ss-band wave dynamics.

6.3. Bulk runup statistics

Observed and modeled bulk runup statistics, including steady wave setup $\langle\eta\rangle$ and sea-swell and infragravity swash height, are compared with all tested boundary conditions. In both model and observations, the runup edge is defined with a 10 cm vertical threshold. Setup is the elevation of the mean runup edge above the still water level, and significant swash height is defined as $\mathrm{S}_{\mathrm{ig/ss}} = 4\sigma_{\mathrm{ig/ss}}$, where $\sigma_{ig/ss}$ is the variance in the infragravity or sea-swell band, following Stockdon et al. (2006). Shoreline setup is defined relative to the water level at P8 (the most offshore P gage, Figure 1).

Setup is well-predicted and does not depend on offshore boundary conditions. For all 19 test cases, modeled (with all BC) and observed setup are within 7%, with a typical difference of 9. cm (not shown). Modeled and observed sea-swell swash height S_{ss} are always small ($< 0.2\,\mathrm{m}$), with modeled S_{ss} differing by only

2.4 cm (not shown). Infragravity swash height S_{ig} for different BC typically span a larger range 30 cm (Figure 7a), about 30% of the typical 1 m S_{ig}. For the default model friction, Manning's roughness coefficient $n = 0.019$, the bound wave BC performs best. However, an analysis of covariance (ANCOVA) test for total runup, defined as $\langle\eta\rangle + S/2$, with $S = \sqrt{S_{ig}^2 + S_{ss}^2}$, shows the models do not differ statistically from each other with 95% confidence.

Modeled infragravity runup predictions are sensitive to friction, as shown for the Fourier PU BC (Figure 7b). The n values, between 0.016 and 0.025, are within the range typically used in surf zone modeling (e.g. Apotsos et al., 2007; Smit et al., 2013). Improved modeling of friction, for example by increasing the number of model layers, and including boundary layers and turbulent mixing, is beyond the present scope.

The present results are applicable to low beach slopes, and the sensitivity to offshore BC could be different on steep beaches when breakpoint generation is important (Battjes et al., 2004). For the practical applications of runup predictions where no observations are available at the offshore boundary, and the erroneous ig physics in the surfzone are not of concern, a boundary condition of 1D boundwaves with n=0.019 is viable. However, Fourier PU is clearly the overall most accurate representation of wave conditions (linear and nonlinear) at the offshore boundary and across the surfzone (Figures 4, 5 and 6).

7. Discussion and Conclusions

In many of the test cases with the preferred PU Fourier boundary conditions, ss shoreward propagating wave heights are accurately predicted through the outer half of the domain, while ig wave heights are over-predicted. Fourier *PU* and Free *PU* reduce the effect of shoreline reflection neglected in the *P*-only estimates, but are $\sim$ 13% higher at the boundary owing to the lack of directional spread in the 1D boundary conditions used here. Furthermore, the lack of directional spread may over-amplify ig wave growth. The ig skewness, asymmetry and biphases for these large wave cases with the Fourier *PU* BC input is generally well-predicted, however, suggesting that errors in energy transfers are large enough to influence wave height but have relatively less effect on normalized moments. The Fourier BCs match well with the observations. Free wave conditions (Free P, Free PU) at the boundary impose Gaussian statistics (Sk = 0) for skewness regardless of Ur. The BC inputs at the boundary therefore perform as expected; free waves should not have any associated skewness as they are fundamentally uncoupled, whereas the prescribed phases Fourier BCs should match exactly the observations. In modeling nonlinear moments, the difference in choice of pressure and current or pressure-only inputs makes little difference.

Accurate representation of both the shoreward energy flux and nonlinear moments allows for more precise interpretation of dynamics both onshore and seaward of the surfzone. Wave shape, and its associated velocity skewness and asymmetry, is thought to strongly influence cross-shore sediment transport (e.g. Hoefel and Elgar, 2003), although the role of infragravity contributions is not well understood. Infragravity sediment flux may depend on the correlation of ig and short waves (Roelvink and Stive, 1989) and relative ig and ss wave heights (e.g. de Bakker et al., 2016). As boundary condition errors propagate into the surfzone (Figure 5), errors in bulk and higher order statistics would affect estimates of both ss and ig sediment transport in both magnitude and direction.

The nonlinear moments of all tested models tended toward collapse to a common solution in the inner surfzone, and modeled bulk runup statistics reveal no statistical difference between the tested boundary conditions. These results suggest a strong local forcing in the surfzone, largely independent of the ig offshore boundary conditions. Closer examination of higher order statistics in the surf and swash zones may further elucidate the dynamics leading to this collapse, as well as the physics of ig-ss interactions in extreme runup.

Acknowledgements

This study was funded by the United States Army Corps of Engineers Coastal Ocean Data Systems Program (W912HZ-14-2-0025), the California Department of Parks and Recreation, Division of Boating and Waterways Oceanography Program (C1370032), and the Southern California Coastal Ocean Observing System (NOAA IOOSREG-T-000-00). Field data was collected with help from Brian Woodward, Bill Boyd, Dennis Darnell, Kent Smith, Rob Grenzeback, Nicholas Spore, Bonnie Ludka, Timu Gallien, and Richie Slocum. Michele Okihiro organized logistics. We thank two anonymous reviewers for insightful suggestions that improved this paper.

Appendix A. Normalization of 3rd order moments

To interpret the strength of the correlation for the ig-ss-ss interaction skewness and asymmetry it is convenient to normalize the results. Here we consider three alternatives: total variance, band variance, and constrained. Normalization with total variance gives

$$\mathrm{Sk}'_{\mathrm{ig,ss,ss}} + i\mathrm{As}'_{\mathrm{ig,ss,ss}} = \frac{3}{2}\frac{\langle \zeta_{\mathrm{ig}}\zeta_{\mathrm{ss}}\zeta^*_{\mathrm{ss}}\rangle}{\langle \eta^2\rangle^{3/2}} \tag{A.1}$$

and typically yields small values at the offshore boundary where $\langle \eta^2_{\mathrm{ig}}\rangle \ll \langle \eta^2_{\mathrm{ss}}\rangle$ (Figure 2b), even if ig and ss waves are (strongly) correlated. Alternatively, normalization by band (rather than total) variance gives

$$\mathrm{Sk}'_{\mathrm{ig,ss,ss}} + i\mathrm{As}'_{\mathrm{ig,ss,ss}} = \frac{3}{2}\frac{\langle \zeta_{\mathrm{ig}}\zeta_{\mathrm{ss}}\zeta^*_{\mathrm{ss}}\rangle}{\langle \eta^2_{\mathrm{ss}}\rangle\sqrt{\langle \eta^2_{\mathrm{ig}}\rangle}} \tag{A.2}$$

This yields higher values even if ig signal is relatively small, but values are still unconstrained.

To constrain normalized skewness and asymmetry, we decompose the third order complex moment as the correlation between zero mean signals A and B, i.e.

$$A = \frac{3}{2}\zeta_{\mathrm{ig}}, \qquad B = \zeta_{\mathrm{ss}}\zeta^*_{\mathrm{ss}} - \langle \zeta_{\mathrm{ss}}\zeta^*_{\mathrm{ss}}\rangle, \tag{A.3}$$

where inclusion of the factor 3/2 in A or B is arbitrary. The real signal B can be interpreted as fluctuations in short wave energy. Since $\langle \zeta_{\rm ig} \langle \zeta_{\rm ss} \zeta_{\rm ss}^* \rangle \rangle = 0$, the third order correlation can be interpreted as a second order cross-correlation between A and B. Further since only low frequency oscillations in $B = B_{\rm ig} + B_{\rm ss}$ that lie in the ig-band can correlate with $\zeta_{\rm ig}$, we find

$$\langle \zeta_{\rm ig} \zeta_{\rm ss} \zeta_{\rm ss}^* \rangle = \langle AB \rangle = \langle AB_{\rm ig} \rangle \tag{A.4}$$

Since the latter is simply a two point correlation between signals A and $B_{\rm ig}$ we can normalized moments analogous to the Pierson correlation coefficient as

$$\mathrm{Sk}'_{\rm ig,ss,ss} + i\mathrm{As}'_{\rm ig,ss,ss} = \frac{\sqrt{2}\langle AB_{\rm ig} \rangle}{\sqrt{\langle AA^* \rangle \langle B_{\rm ig}^2 \rangle}} = \frac{\sqrt{2}\langle \zeta_{\rm ig} \zeta_{\rm ss} \zeta_{\rm ss}^* \rangle}{\sqrt{\langle \zeta_{\rm ig} \zeta_{\rm ig}^* \rangle \langle B_{\rm ig}^2 \rangle}} \tag{A.5}$$

Here skewness and asymmetry are constrained between -1 and 1, and further the bicoherence

$$C_{\rm ig,ss,ss}^2 = \mathrm{Sk}_{\rm ig,ss,ss}^2 + \mathrm{As}_{\rm ig,ss,ss}^2 \tag{A.6}$$

is constrained as $0 \leq C_{\rm ig,ss,ss} \leq 1$. The advantage of this definition is that it filters all irrelevant contributions from the scaling, and produces values close to one if wave groups and ig-waves are strongly coupled regardless of relative magnitude (Figures 2, 5, 6).

References

A. T. M. de Bakker, J. A. Brinkkemper, F. van der Steen, M. F. S. Tissier, B. G. Ruessink, Cross-shore sand transport by infragravity waves as a function of beach steepness, Journal of Geophysical Research F: Earth Surface 121 (2016) 1786–1799.

H. F. Stockdon, R. a. Holman, P. a. Howd, A. H. Sallenger, Empirical parameterization of setup, swash, and runup, Coastal Engineering 53 (2006) 573–588.

P. Ruggiero, R. A. Holman, R. A. Beach, Wave run-up on a high-energy dissipative beach, Journal of Geophysical Research 109 (2004) C06025.

M. S. Longuet-Higgins, R. W. Stewart, Radiation stress and mass transport in gravity waves, with application to 'surf beats', Journal of Fluid Mechanics 13 (1962) 481.

K. Hasselmann, On the non-linear energy transfer in a gravity-wave spectrum, Journal of Fluid Mechanics 12 (1962) 481–500.

J. Kostense, Measurements of surf beat and set-down beneath wave groups, in: 19th International Conference on Coastal Engineering, 1985, pp. 724–740. doi:10.1061/9780872624382.050.

D. P. Rijnsdorp, P. B. Smit, M. Zijlema, Non-hydrostatic modelling of infragravity waves under laboratory conditions, Coastal Engineering 85 (2014) 30–42.

A. T. M. de Bakker, T. H. C. Herbers, P. B. Smit, M. F. S. Tissier, B. G. Ruessink, Nonlinear Infragravity–Wave Interactions on a Gently Sloping Laboratory Beach, Journal of Physical Oceanography 45 (2015) 589–605.

A. Torres-Freyermuth, J. L. Lara, I. J. Losada, Numerical modelling of short- and long-wave transformation on a barred beach, Coastal Engineering 57 (2010) 317–330.

A. T. M. de Bakker, M. F. S. Tissier, G. Ruessink, Shoreline dissipation of infragravity waves, Continental Shelf Research 72 (2014) 73–82.

A. Ruju, J. L. Lara, I. J. Losada, Numerical analysis of run-up oscillations under dissipative conditions, Coastal Engineering 86 (2014) 45–56.

P. Higuera, J. L. Lara, I. J. Losada, Realistic wave generation and active wave absorption for Navier-Stokes models. Application to OpenFOAM®., Coastal Engineering 71 (2013a) 102–118.

P. Higuera, J. L. Lara, I. J. Losada, Simulating coastal engineering processes with OpenFOAM®, Coastal Engineering 71 (2013b) 119–134.

P. Higuera, I. J. Losada, J. L. Lara, Three-dimensional numerical wave generation with moving boundaries, Coastal Engineering 101 (2015) 35–47.

J. Orszaghova, P. H. Taylor, A. G. L. Borthwick, A. C. Raby, Importance of second-order wave generation for focused wave group run-up and overtopping, Coastal Engineering 94 (2014) 63–79.

P. D. Bromirski, O. V. Sergienko, D. R. MacAyeal, Transoceanic infragravity waves impacting antarctic ice shelves, Geophysical Research Letters 37 (2010).

F. Ardhuin, A. Rawat, J. Aucan, A numerical model for free infragravity waves: Definition and validation at regional and global scales, Ocean Modelling 77 (2014) 20–32.

T. H. C. Herbers, S. Elgar, R. T. Guza, Generation and propagation of infragravity waves, Journal of Geophysical Research 100872 (1995) 863–24.

P. B. Smit, T. T. Janssen, T. H. C. Herbers, T. Taira, B. A. Romanowicz, Infragravity Wave Radiation Across the Shelf Break, Journal of Geophysical Research: Oceans (2018).

R. T. Mccall, G. Masselink, T. G. Poate, J. A. Roelvink, L. P. Almeida, M. Davidson, P. E. Russell, Modelling storm hydrodynamics on gravel beaches with XBeach-G, Coastal Engineering 91 (2014) 231–250.

E. R. Gomes, R. P. Mulligan, K. L. Brodie, J. E. McNinch, Bathymetric control on the spatial distribution of wave breaking in the surf zone of a natural beach, Coastal Engineering 116 (2016) 180–194.

A. Nicolae Lerma, R. Pedreros, A. Robinet, N. Senechal, Simulating wave setup and runup during storm conditions on a complex barred beach, Coastal Engineering 123 (2017) 29–41.

A. Van Dongeren, R. Lowe, A. Pomeroy, T. M. Duong, D. Roelvink, G. Symonds, R. Ranasinghe, Modelling Infragravity Waves and Currents

Across a Fringing Coral Reef, Coastal Engineering Proceedings 1 (2012) 1–10.

A. A. van Rooijen, R. T. McCall, J. S. Van Thiel de Vries, A. van Dongeren, A. J. Reniers, J. A. Roelvink, Modeling the effect of wave-vegetation interaction on wave setup, Journal of Geophysical Research: Oceans (2016) 4341–4359.

P. V. Guimarães, L. Farina, E. Toldo, G. Diaz-Hernandez, E. Akhmatskaya, Numerical simulation of extreme wave runup during storm events in Tramandai Beach, Rio Grande do Sul, Brazil, Coastal Engineering 95 (2015) 171–180.

T. W. Gallien, Validated coastal flood modeling at Imperial Beach, California: Comparing total water level, empirical and numerical overtopping methodologies, Coastal Eng. 111 (2016) 95–104.

M. Zijlema, G. Stelling, P. Smit, SWASH: An operational public domain code for simulating wave fields and rapidly varied flows in coastal waters, Coastal Engineering 58 (2011) 992–1012.

J. W. Fiedler, K. L. Brodie, J. E. McNinch, R. T. Guza, Observations of runup and energy flux on a low-slope beach with high-energy, long-period ocean swell, Geophys. Res. Lett. 42 (2015) 9933–9941.

T. H. C. Herbers, S. Elgar, R. T. Guza, Directional spreading of waves in the nearshore zone, Journal of Geophysical Research 104 (1999) 7683–7693.

T. C. Lippmann, T. H. Herbers, E. B. Thornton, Gravity and shear wave contributions to nearshore infragravity motions, Journal of Physical Oceanography 29 (1999) 231–239.

F. Ursell, Edge waves on a sloping beach, Proceedings Of The Royal Society Of London Series A-Mathematical And Physical Sciences 214 (1952) 79–97.

A. Sheremet, R. T. Guza, T. H. C. Herbers, A new estimator for directional properties of nearshore waves, Journal of Geophysical Research: Oceans 110 (2005) 1–11.

Y. C. Kim, E. J. Powers, Digital Bispectral Analysis and Its Applications to Nonlinear Wave Interactions, IEEE Transactions on Plasma Science 7 (1979) 120–131.

S. Elgar, R. T. Guza, Observations of bispectra of shoaling surface gravity waves, Journal of Fluid Mechanics 161 (1985a) 425–448.

S. Elgar, R. T. Guza, Shoaling gravity waves : comparisons between field observations, linear theory, and a nonlinear model, Journal of Fluid Mechanics 158 (1985b) 47–70.

T. H. C. Herbers, M. C. Burton, Nonlinear shoaling of directionally spread waves on a beach, Journal of Geophysical Research: Oceans 102 (1997) 21101–21114.

J. Thomson, S. Elgar, B. Raubenheimer, T. H. C. Herbers, R. T. Guza, Tidal modulation of infragravity waves via nonlinear energy losses in the surfzone, Geophysical Research Letters 33 (2006) L05601.

R. Guedes, K. R. Bryan, G. Coco, Observations of wave energy fluxes and swash motions on a low-sloping, dissipative beach, Journal of Geophysical Research: Oceans 118 (2013) 3651–3669.

A.-C. N. Pequignet, J. M. Becker, M. A. Merrifield, Energy transfer between wind waves and low-frequency oscillations on a fringing reef, Ipan, Guam, Journal of Geophysical Research: Oceans 119 (2014) 6709–6724.

A. Masuda, Y. Y. Kuo, Bispectra for the surface displacement of random gravity waves in deep water, Deep Sea Research Part A, Oceanographic Research Papers 28 (1981) 223–237.

J. W. Fiedler, P. B. Smit, K. L. Brodie, J. McNinch, R. T. Guza, Numerical modeling of wave runup on steep and mildly sloping natural beaches, Coastal Engineering 131 (2018) 106–113.

J. A. Bailard, D. L. D. L. Inman, An Energetics Bedload Model for Plane Sloping Beach: Local Transport, Journal of Geophysical Research 86 (1981) 2035–2043.

F. Hoefel, S. Elgar, Wave-Induced Sediment Transport and Sandbar Migration, Science 299 (2003) 1885–1887.

S. M. Henderson, R. T. Guza, S. Elgar, T. H. C. Herbers, A. J. Bowen, Nonlinear generation and loss of infragravity wave energy, Journal of Geophysical Research: Oceans 111 (2006) C12007.

W. E. Rogers, G. P. Van Vledder, Frequency width in predictions of windsea spectra and the role of the nonlinear solver, Ocean Modelling 70 (2013) 52–61.

A. Apotsos, B. Raubenheimer, S. Elgar, R. T. Guza, J. A. Smith, Effects of wave rollers and bottom stress on wave setup, J. Geophys. Res. 112 (2007) C02003–10.

P. Smit, M. Zijlema, G. Stelling, Depth-induced wave breaking in a non-hydrostatic, near-shore wave model, Coastal Engineering 76 (2013) 1–16.

J. A. Battjes, H. J. Bakkenes, T. T. Janssen, A. van Dongeren, Shoaling of subharmonic gravity waves, Journal of Geophysical Research 109 (2004) 1–15.

J. A. Roelvink, M. J. F. Stive, Bar-generating cross-shore flow mechanisms on a beach, Journal of Geophysical Research 94 (1989) 4785.

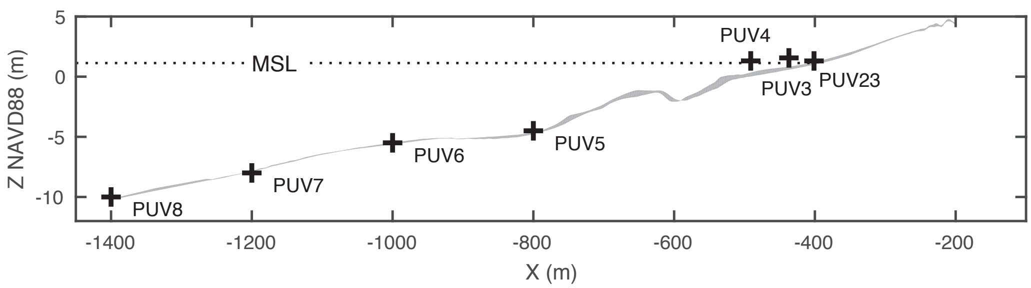

Figure 1: Agate Beach, Oregon: depth versus cross-shore distance, with co-located pressure sensor and current meter locations.

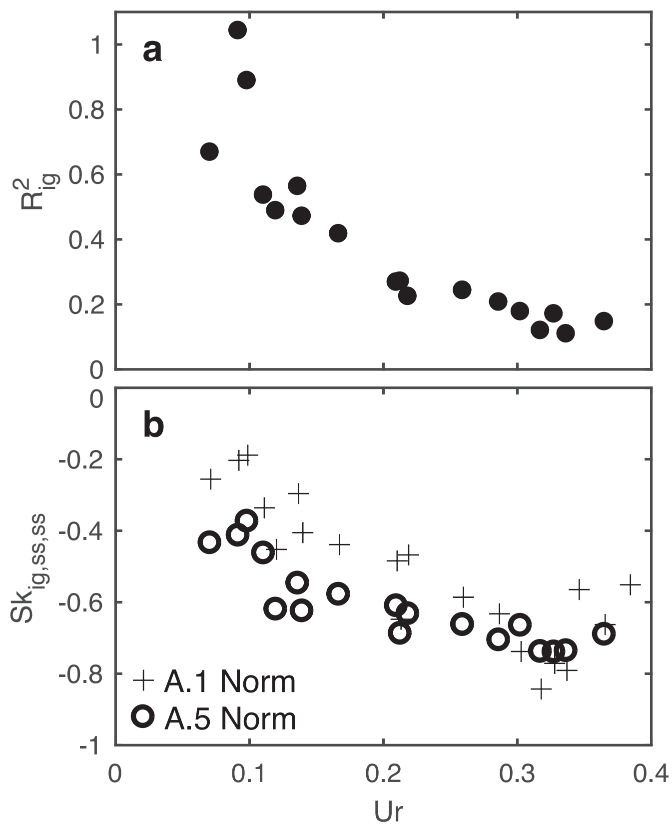

Figure 2: At the offshore boundary (a) Infragravity reflection coefficient R^2_{ig} and (b) interaction skewness versus Ursell number Ur (1). Data skewness normalizations are to total skewness (+, A.1, multiplied by 4 for visibility), and constrained (circles, A.5). Normalized skewness constrained between +1 and -1 (equation A.5) is used below.

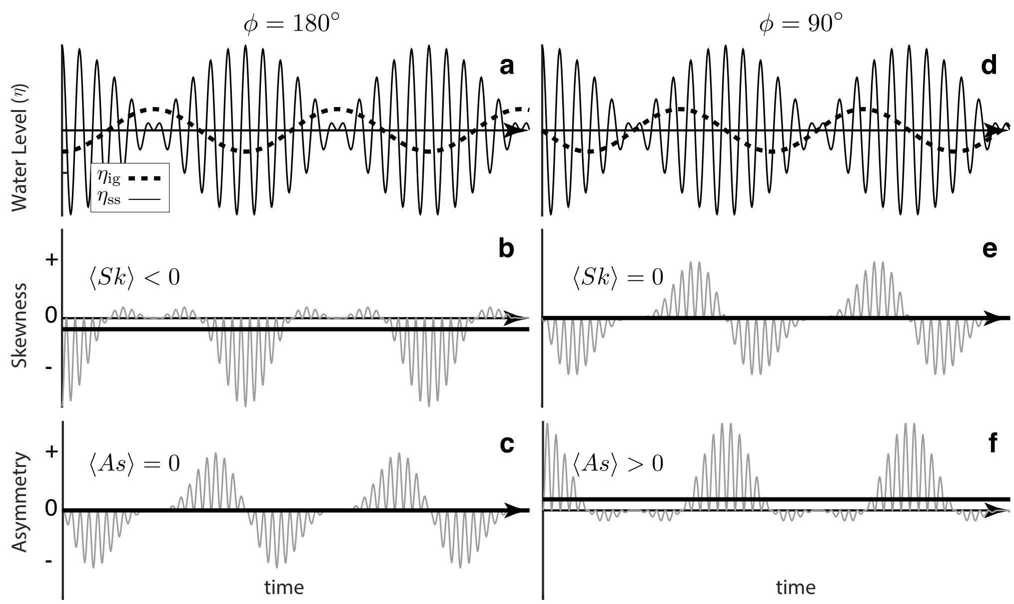

Figure 3: (a,d) Water elevations versus time for a short wave group (η_{ss}) and a long wave (η_{ig}). Units are arbitrary. Biphase ϕ is (left) 180° and (right) 90°. The ss waves are equal amplitude sinusoids at f and $f + df$, with the (exaggerated) ig wave at frequency df. Infragravity and ss waves are themselves not skewed or asymmetric ($\mathrm{Sk}_{ig,ig,ig} = \mathrm{As}_{ig,ig,ig} = \mathrm{Sk}_{ss,ss,ss} = \mathrm{As}_{ss,ss,ss} = 0$.) (b,e) Instantaneous interaction ig-ss-ss skewness term $3\eta_{ig}\eta_{ss}^2 = \frac{3}{2}\Re\langle\zeta_{ig}\zeta_{ss}\zeta_{ss}^*\rangle$ versus time, with the time average (= $\mathrm{Sk}_{ig,ss,ss}$) shown by the solid bold line. (c,f) Instantaneous interaction asymmetry $\frac{3}{2}\Im\langle\zeta_{ig}\zeta_{ss}\zeta_{ss}^*\rangle$ versus time (time average, bold line). The instantaneous skewness and asymmetry (b,c,e,f) contain low and high frequency terms, and a mean.

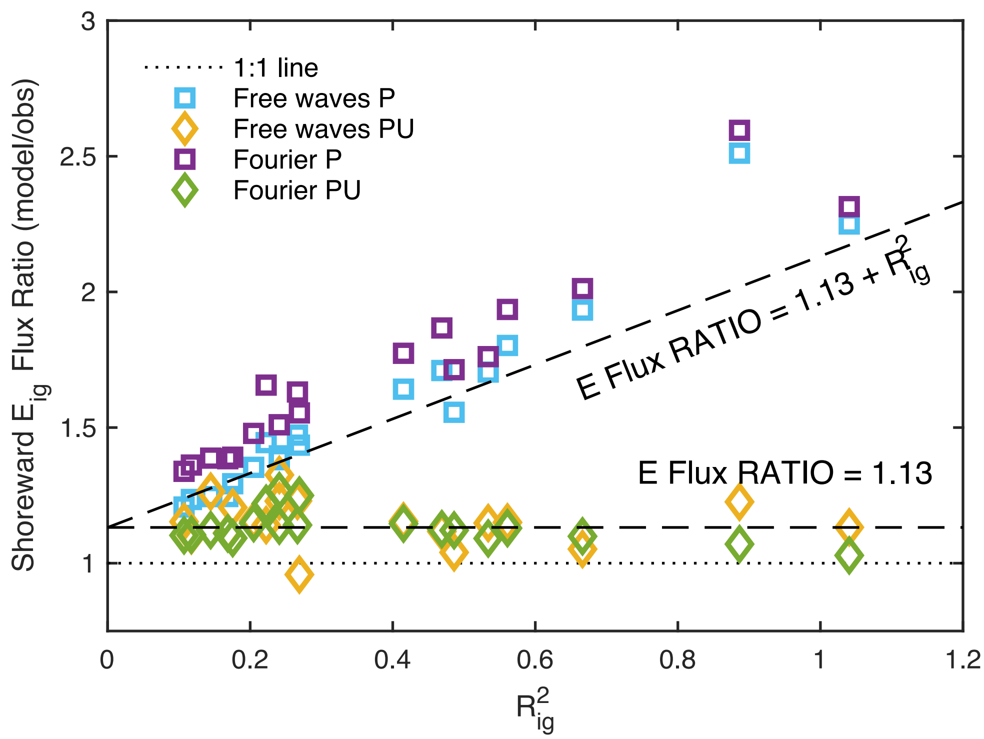

Figure 4: Modeled ig shoreward energy flux (normalized by observed) versus ig reflection coefficient R^2_{ig}, both at the offshore boundary, for different boundary conditions (see legend). Boundary conditions using pressure P only (squares) neglect shoreline reflection, and overestimate the shoreward energy flux by a factor of $(1.13 + R^2_{\text{ig}})$. Using the cross-shore velocity (U) in the boundary condition (diamonds, Fourier PU and Free PU) includes reflection, and is more accurate. The small (13%) overestimation with PU is owing to satisfying the 1D model assumption of normally incident waves, and neglecting wave directionality that is included in the observed estimate. Linear flux estimates are not affected by differences between free and Fourier boundary conditions.

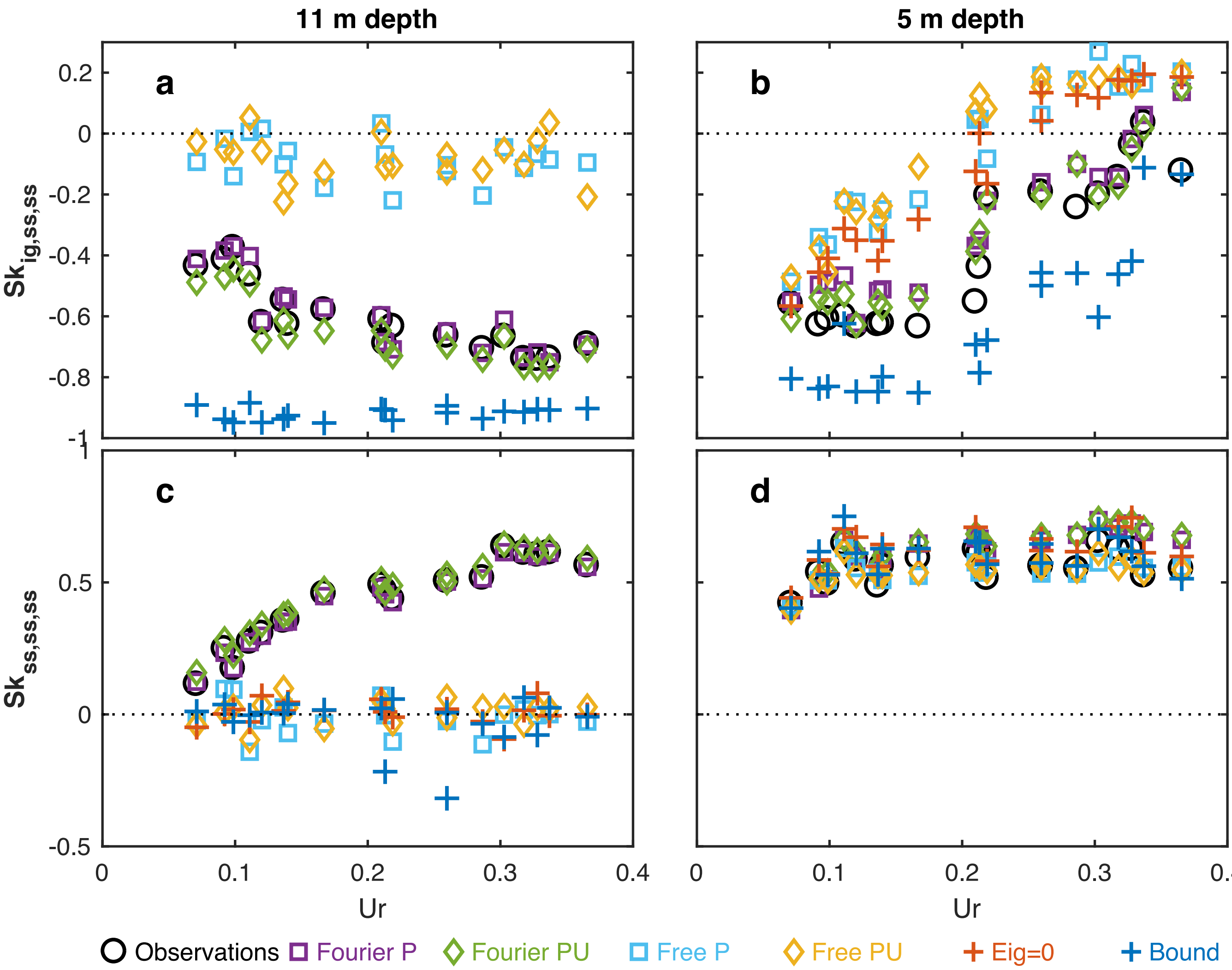

Figure 5: Skewness of the shoreward propagating signal at the boundary (11 m depth, left) and mid-array (5 m depth, right) for (a,b) $\mathrm{Sk}_{\mathrm{ig,ss,ss}}$and (c,d) $\mathrm{Sk}_{\mathrm{ss,ss,ss}}$. Symbols correspond to different boundary conditions (legend). At the boundary (a,c), free wave boundary conditions yield Gaussian statistics (skew= 0), whereas observed Fourier boundary conditions (P and PU) match the observed skewness (black circles). Difference interaction skewness (a,b) is constrained between -1 and 1 (A.5), and self interaction skewness (c,d) is normalized to the total variance. $\mathrm{Sk}_{\mathrm{ig,ss,ss}}$ for E_{ig} is undefined at the boundary, and not shown.

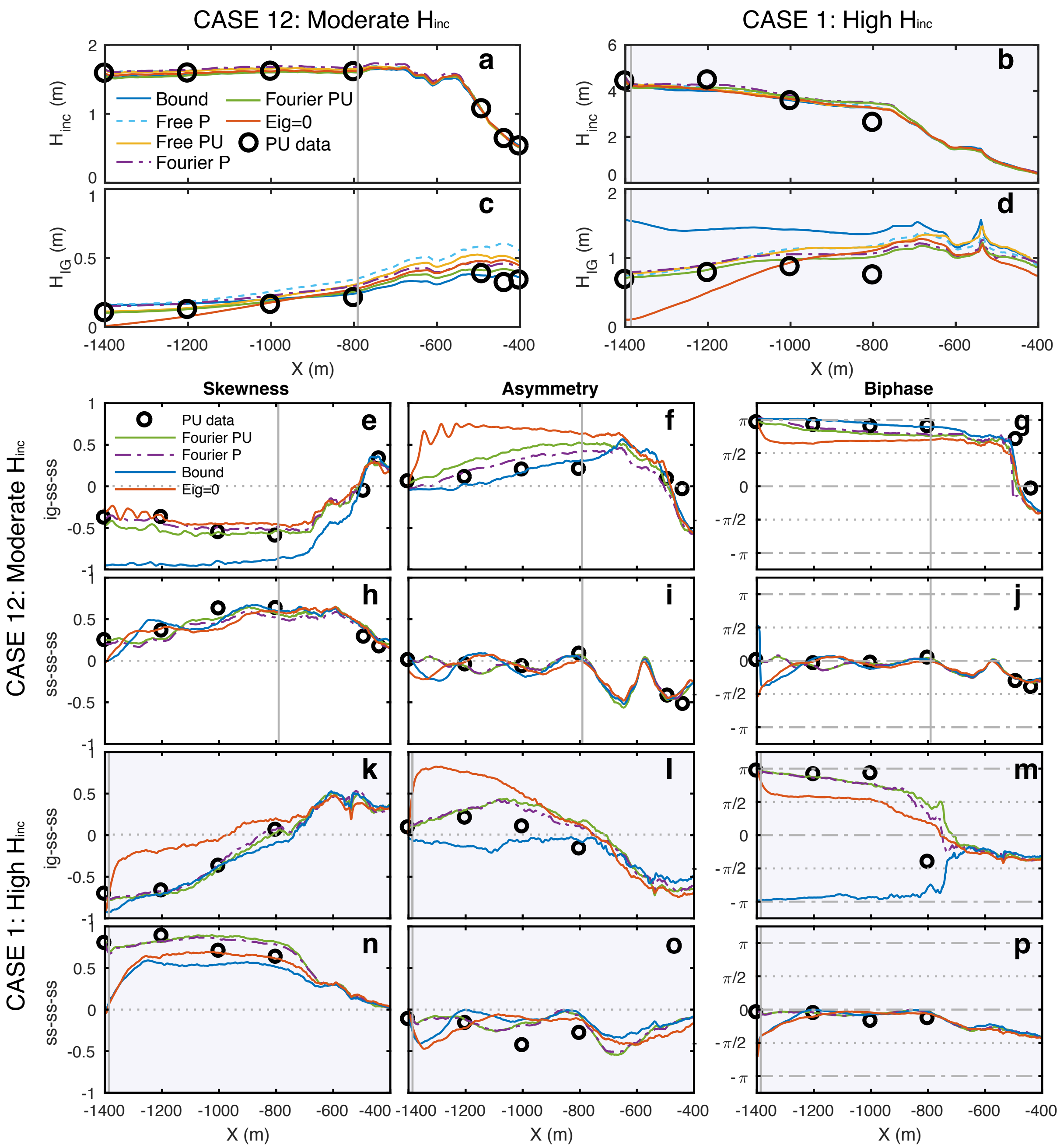

Figure 6: Shoreward propagating (a,b) incident and (c,d) infragravity wave heights versus cross-shore distance x with (left) moderate and (right) high wave energy. (e-p) Nonlinear moments of shoreward propagating waves versus cross-shore distance. Moments: (left) skewness Sk (center) asymmetry As and (right) biphase ϕ. Sk and As are normalized to between -1 and 1 for the ig-ss-ss sub-band and to total variance for ss-ss-ss. High energy panels are shaded gray. Line types correspond to initial conditions (legend in (a)). Model data in water depths less than 0.75 m are not shown.

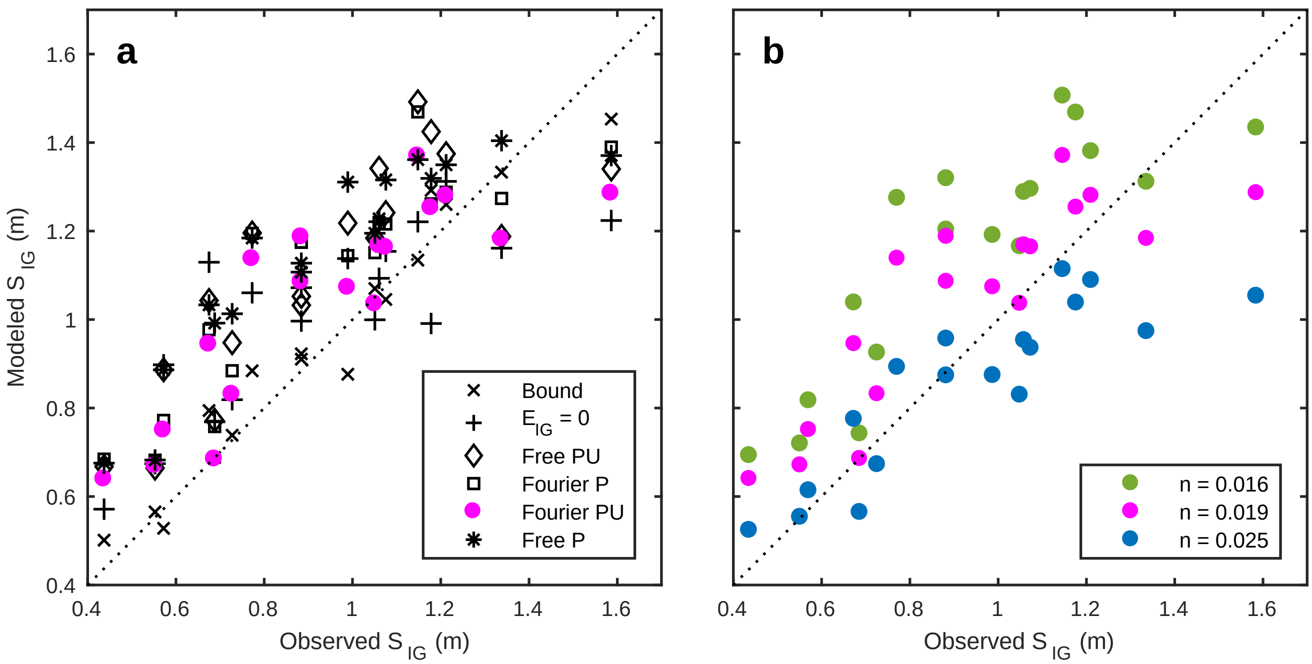

Figure 7: Modeled vs observed bulk infragravity swash S_{ig} for (a) tested boundary conditions (symbols in legend) with default friction coefficient (n=0.019) and (b) Fourier PU BC with varied friction parameters (legend). Dotted black line is the 1:1 line of model-observation agreement.